trons cm^{-2} s^{-1} MeV^{-1}, that is, below the detector threshold ($\sim 1 \times 10^{-2}$), at $\Delta\phi$ = 11.2° where SMM crossed the shell. Flux levels of 1×10^{-2} are found at $\Delta\phi \approx 14°$ and 29° on the 160-s shell; flux levels of 2×10^{-2} are found at $\Delta\phi \approx 28°$ and 22°.

The results of this analysis and comparable analyses of other *L*-shells are shown in the top panel of Fig. 5. For six times from 16:39:08 to 16:40:40 UT the drift longitudes of the peak flux and of flux levels 1, 2, and 5×10^{-2} positrons cm^{-2} s^{-1} MeV^{-1} on the shells being crossed by SMM were determined from Fig. 4. The isoflux contours joining these points, drawn in Fig. 5, trace the evolution, not on a single *L*-shell, but of the positron intensity distributions on successive shells as SMM crossed them. Thus, after ~16:38:50 UT SMM was on shells that contained positrons, but it was not until ~16:39:40 that it encountered a shell on which the positron flux, at the point of crossing, had reached detector threshold levels. The peak flux ($\sim 3.5 \times 10^{-2}$ cm^{-2} s^{-1} MeV^{-1}) was encountered on another shell at ~16:40:04 and after ~16:40:40, SMM was on shells whose positrons had mostly drifted westward of its crossing point.

In the bottom panel of Fig. 5 a dashed curve shows the theoretical count rate profile of the event corresponding to the contour-crossing history in the top panel. Also shown is the observed count rate profile consisting of the five 16.38-s count bins that were above threshold. Our analysis predicts a peak count rate about half that observed, occurring about 20 s after the observed peak time. These differences are easily ascribed to uncertainties in the orbital and physical features of Cosmos as well as to inaccuracies of the model and calculations.

The *L*-shell positions and geomagnetic longitudinal separations of SMM and Cosmos 1176 have been examined for times surrounding all of the events depicted in Fig. 1, although a detailed analysis such as that for event 5 was not done. It was found that the onset times of nearly all the events were consistent with the interception by SMM of ~1- to 5-MeV positrons drifting westward from Cosmos 1176. These many analyses, together with the detailed analysis of event 5 and the qualitative arguments presented earlier with regard to Fig. 1, show that all of the essential features of the SMM 511-keV gamma events can be explained as due to positrons from Cosmos 1176.

REFERENCES AND NOTES

1. *Aviat. Week Space Technol.* (30 January 1978), p. 33.
2. B. M. Jasani, *Outer Space–Battlefield of the Future?*, (Crane, Russak & Co., New York, 1978).
3. *TRW Space Log*, (TRW Space & Technology Group, Redondo Beach, CA, 1978), vol. 23.
4. E. Rieger *et al.*, *Science* **244**, 441 (1989).
5. G. H. Share, J. D. Kurfess, K. W. Marlow, D. C. Messina, *ibid.*, p. 444.
6. E. W. Hones, *J. Geophys. Res.* **69**, 182 (1964).
7. M. Schulz and L. J. Lanzerotti, *Particle Diffusion in the Radiation Belts* (Springer-Verlag, New York, 1974), p. 22.
8. T. G. Northrop and E. Teller, *Phys. Rev.* **117**, 215 (1960).
9. C. E. McIlwain, *J. Geophys. Res.* **66**, 3681 (1961).
10. F. C. Maienschein, R. W. Peele, W. Zober, T. A. Love, in *Proceedings of the Second International United Nations Conference on Peaceful Uses of Atomic Energy* (United Nations, Geneva, 1958), vol. 15, p. 366.
11. R. D. Evans, *The Atomic Nucleus* (McGraw-Hill, New York, 1955), p. 703.
12. N. C. Christofilos, *J. Geophys. Res.* **64**, 869 (1959).
13. J. A. Welch, Jr., and W. A. Whitaker, *ibid.*, p. 909.
14. H. Kallmann-Bijl *et al.*, *COSPAR International Reference Atmosphere 1961* (North-Holland, Amsterdam, 1961).
15. R. E. Wiley and F. D. Barish, *Technical Report no. AFWL-TR-69-114*, (Air Force Weapons Laboratory, Kirtland AFB, NM, 1970).
16. We thank the North American Aerospace Defense Command (NORAD) for providing us the orbital elements for the SMM and Cosmos 1176 satellites. This work was done under the auspices of the U.S. Department of Energy.

2 March 1989; accepted 23 March 1989

Observations of Nuclear Reactors on Satellites with a Balloon-Borne Gamma-Ray Telescope

TERRENCE J. O'NEILL, ALAN D. KERRICK, FARID AIT-OUAMER, O. TUMAY TUMER, ALLEN D. ZYCH, R. STEPHEN WHITE

Gamma rays at energies of 0.3 to 8 megaelectron volts (MeV) were detected on 15 April 1988 from four nuclear-powered satellites including Cosmos 1900 and Cosmos 1932 as they flew over a double Compton gamma-ray telescope. The observations occurred as the telescope, flown from a balloon at an altitude of 35 kilometers from Alice Springs, Australia, searched for celestial gamma-ray sources. The four transient signals were detected in 30 hours of data. Their time profiles show maxima with durations of (21 ± 1) and (27 ± 1) seconds (half-width at half maximum) for the lower two satellites and (85 ± 5) and (113 ± 7) seconds for the remaining two. Their durations place the origin of the two shorter signals at orbital radii of 260^{+40}_{-60} and 260 ± 60 km above the earth and the two longer at 800^{+100}_{-300} and 800^{+250}_{-300} kilometers. Their luminosities for energies >0.3 MeV are then $(6.1 \pm 1.5) \times 10^{15}$, $(3.9 \pm 1.0) \times 10^{15}$, $(1.10 \pm 0.28) \times 10^{16}$, and $(1.30 \pm 0.32) \times 10^{16}$ photons per second. The imaging of the strongest signal indicates a southeastern direction passing nearly overhead. The energy spectrum can be fit to an exponential with index 2.4 ± 1.4. These transient events add to the already large backgrounds for celestial gamma ray sources.

RECENT ARTICLES HAVE DISCUSSED background signals observed by Solar Maximum Mission and Ginga satellite instruments that appear to be caused by nuclear reactors on Soviet satellites (*1, 2*). These signals are produced by electrons and positrons emitted by the hull of the reactor then trapped temporarily in specific regions of the earth's magnetic field. Computer memories of scientific instruments on satellites that fly through these regions are filled, preventing the detection of celestial radiation. Suggestions have been made to shut down instruments on NASA's Gamma Ray Observatory (GRO), which will be launched into earth orbit in the near future, as it passes through these regions or to disregard the radiation when simultaneously detecting electrons or positrons. Direct gamma-ray emission may also cause a significant increase in the background radiation.

Here we report the detection of direct gamma-ray emission from four different satellite reactors. The observations were made during a 30-hour period with the University of California, Riverside (UCR), double Compton telescope launched from a balloon to an altitude of 35 km. We observed two satellites at 260-km altitude and two at 800 km, the latter above the future orbit of GRO. The flux we detected from the nearest reactor exceeded by 50 times the flux expected from the strongest celestial sources. The Comptel experiment on GRO, which is similar to our instrument and which possesses a large field of view and high sensitivity, could also be subjected to these enormous signals (*3*).

The UCR double Compton telescope (*4, 5*) was designed to search for celestial gamma-ray sources at energies of 1 to 30 MeV. Because the aperture of the instrument is about 1 steradian, virtually the entire southern sky could be searched in 24 hours from Alice Springs, Australia.

Department of Physics and Institute of Geophysics and Planetary Physics, University of California, Riverside, CA 92521.

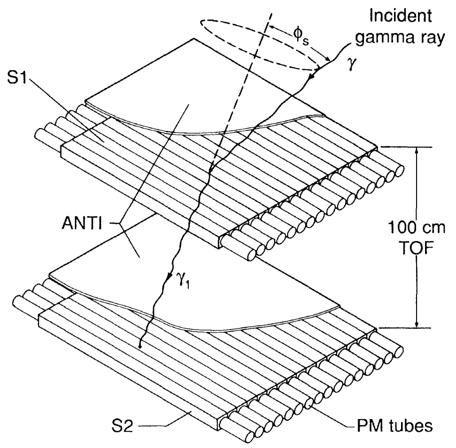

Fig. 1. The UCR double scatter Compton telescope. An incident gamma-ray γ Compton scatters from an electron in the top plastic scintillation array (6.35 cm by 7.62 cm by 103 cm, 16 units) depositing its energy in S1. The gamma ray, γ_1, continues on to the lower array S2 (4.83 cm by 4.83 cm by 102 cm, 16 units) where it is completely absorbed in the denser material. Because the scattered electron direction in S1 is not measured, a ring in the sky is obtained for the possible incident gamma-ray directions. The anticoincidence sheets (ANTI) on the top and bottom of each array eliminate charged particles. TOF refers to time of flight and PM to photomultiplier tubes.

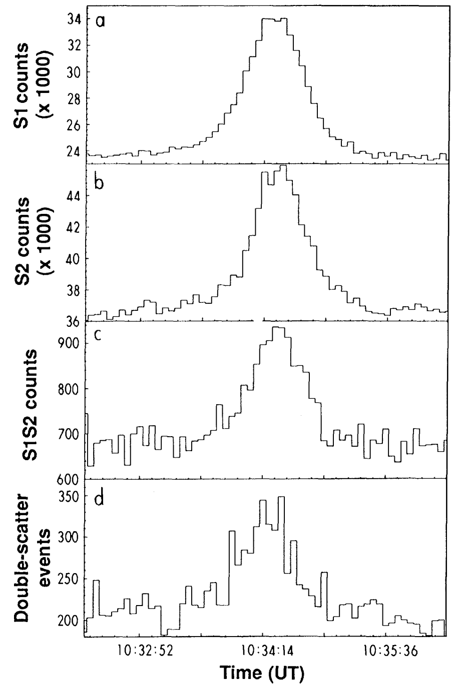

Fig. 2. Count rate profiles of satellite A for the (**a**) top array (S1), (**b**) bottom array (S2), (**c**) their coincidences (S1S2), and (**d**) telescope double scatters. The channel widths are 4.096 s with the peak occurring at 10:34:20 UT.

Fig. 3. Contour sky map of gamma rays from satellite A. The gamma-ray event rings were summed over the duration of the event. The grid is 15° by 15° in right ascension and declination. The telescope zenith is depicted by the black square. The plot shows the satellite nearly overhead moving from northwest toward the southeast.

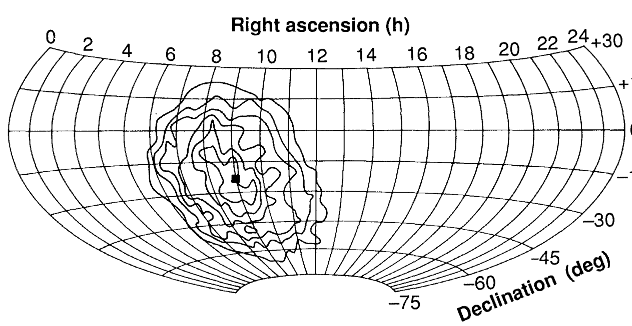

The telescope consists of two scintillation arrays of 1-m^2 area each separated by 1 m as shown in Fig. 1. The top array (S1) of 1.05-m^2 area consists of 16 plastic 6.35 cm by 7.62 cm by 103 cm scintillation bars with photomultiplier tubes attached at both ends. The bottom array (S2) of 0.721 m^2-area has sixteen 4.83 cm by 4.83 cm by 102 cm NaI (Tl) scintillation bars. The energy thresholds are 0.3 MeV for the top array and 1 MeV for the bottom. The instrument's large aperture and high sensitivity are unique for detecting celestial events as well as satellite reactors.

An incident gamma ray undergoes Compton scattering from an electron in a single bar in the top array and then interacts in the bottom array. The scatter position is determined in the top bar by the time difference in arrival of the light signal at each end, and in the bottom bar by the difference in pulse heights. Each array is sandwiched between thin sheets of plastic scintillator for charged particle anticoincidence. The time of flight between the upper and lower arrays discriminates against neutrons, accidental events, and upward moving gamma rays. From the energy losses and interaction positions in the two scintillator arrays, the angle of an event ring, with all possible directions of the incident gamma ray, is calculated by

$$\cos \phi_s = 1 - m_0c^2 \left(\frac{1}{E_2} - \frac{1}{(E_1 + E_2)}\right) \quad (1)$$

where E_1 and E_2 are the energy losses in the top and bottom arrays, ϕ_s is the scatter angle in the first array, and m_0c^2 is the electron rest mass energy.

In addition, total gamma-ray counts in the upper array (S1), the lower array (S2), and coincidence rate (S1S2) are continuously scanned and telemetered every 5.12 ms. Although this data set contains no spatial or spectral information, the high efficiency makes it ideal for gamma-ray burst searches. During these searches the signals from the satellite reactors were discovered.

At 21:00 universal time (UT) 14 April 1988 the UCR telescope was launched on a balloon from Alice Springs, Australia, to search for gamma-ray sources with energies from 1 to 30 MeV. Float altitude of 35 km was reached at 0:00 UT on 15 April with observations lasting until 6:00 UT 16 April. At 7:21 UT 15 April a short transient signal lasting (27 ± 1) s HWHM (half width at half maximum) was simultaneously observed in the three burst counters. The significances of the count rates in the upper array, lower array, and their coincidences were 50 σ, 40 σ, and 10 σ, where σ is the standard deviation of fluctuations in the background. At 10:34 UT similar signals with (21 ± 1) s HWHM durations gave significances of 150 σ, 100 σ, and 24 σ, respectively. A total of 130,000 excess counts were recorded in the top array, 90,000 in the bottom array, and 2,400 in the coincidence counter in 90 s for the 10:34 UT (satellite A) event. These are by far the largest signals detected by our instrument at float altitude. By comparison the strongest celestial source of gamma rays, which originates within the Crab nebula, accounts for only 3,000 events in the top array for the same time period. Figure 2, a through c, shows the count rate profiles of satellite A for the S1, S2, and the S1S2 counters. The time profiles for the earlier event at 7:21 UT (satellite B) were similar to these. Figure 2d shows the normal telescope count rate for satellite A. During the 90-s time window 1,200 photons above background were measured. These gamma rays are our primary data and contain spatial and spectral information.

Figure 3 shows a contour sky map of all events within the time interval of maximum emission given in Fig. 2d. All gamma-ray event rings were summed throughout the time interval. The instrument's zenith, shown by a box in the figure, was located at right ascension 9 hours and declination −23°. Contour maps of events within the first half of the satellite's passage places it toward the northwest and in the second half toward the southeast. An energy spectrum of the reactor was obtained from a background subtraction between the 1-min interval from 10:34:00 UT to 10:35:00 UT, which contains both source and background events, and a similar time from 10:30:00 UT to 10:31:00 UT containing only background events (Fig. 4). The data points are fit by least squares with an exponential of the form $\exp(-E/E_0)$ where $E_0 = 2.4 \pm 1.4$. This is considerably flatter than the prompt

Table 1. Properties of the observed satellites. Times are UT 15 April 1988. Fluxes are given for satellite distances of closest approach. The errors in luminosity are 1 standard deviation assuming the nominal satellite heights h and angles α.

Satellite	Time of closest approach	Height of telescope b (km)	Telescope longitude	Telescope latitude	Height of satellite h (km)	α (deg)	Flux at the telescope (photons cm^{-2} s^{-1}) >0.3 MeV	Luminosity (10^{15} photons s^{-1}) >0.3 MeV	Identity
A	10:34:20	36.5	134°13.5'E	22°51.3'S	260^{+40}_{-60}	10 ± 10	0.96 ± 0.24	6.1 ± 1.5	RORSAT Cosmos 1900 or 1932
B	07:21:58	36.6	134°47.1'E	23°17.3'S	260 ± 60	35 ± 10	0.41 ± 0.110	3.9 ± 1.0	The other of above
C	23:45:54	37.3	131°55.3'E	24°03.1'S	800^{+100}_{-300}	25 ± 10	0.113 ± 0.028	11.0 ± 2.8	An advanced-type reactor
D	09:12:43	36.2	134°33.0'E	22°53.4'S	800^{+250}_{-300}	43 ± 10	0.086 ± 0.021	13.0 ± 3.2	An advanced-type reactor

^{235}U fission gamma spectrum, which has the form $\exp(-E/0.926)$ (6). The flattening could result from the larger attenuation of the lower energy gamma rays before escaping from the reactor.

Smaller signals were detected at 9:12 UT (satellite D) and 23:45 UT (satellite C). Their longer durations, lower peak fluxes, and Gaussian signatures suggest nuclear-powered satellites with orbital radii larger than satellites A and B. The duration of the 9:12 UT event was (113 ± 10) s HWHM with significances of 25 σ and 15 σ in the top and bottom arrays. Similarly, the duration of the 23:45 UT event was (85 ± 5) s HWHM with significances of 75 σ and 17 σ.

The measured satellite reactor time profiles are very different from solar flares or gamma-ray bursts. Celestial events usually show a large variation with gamma-ray bursts having rise times of fractions of seconds and time durations of seconds, whereas the satellite reactors give longer, more symmetric signals, particularly in the S1 array with its lower energy thresholds. At an altitude of 260 km, or 225 km above the telescope, a satellite's time profile is calculated to be 21 s HWHM for a passage directly overhead. At 30° for the zenith angle of closest approach the duration increases to 30 s HWHM. The time profile seen from a gamma-ray telescope onboard a satellite tends to be shorter because of the larger relative velocities between the spacecraft. Satellite instruments also see the 0.511-MeV gamma rays created by reactor-produced positrons that annihilate in the vicinity of the instrument.

The expected flux, F_θ, of gamma rays from a satellite reactor at zenith angle, θ, is

$$F_\theta = F_0 \cos^3\theta \exp\left[-\frac{g}{\lambda}\left(\frac{1}{\cos\theta} - 1\right)\right] \quad (2)$$

where F_0 is the flux for the satellite directly overhead, g is the amount of atmosphere above the balloon telescope, 4 g/cm^2, and λ is the mean free path for gamma-ray absorption in air, 40 g/cm^2, at 2 MeV. The $\cos\theta$ is related to the heights of the satellite and balloon above the earth, h and b, the projected horizontal nearest distance of approach of the satellite to the balloon, a, the satellite velocity, v, assuming a circular orbit and the time from the position of nearest approach, t, by

$$\cos\theta = \frac{h-b}{[(h-b)^2 + a^2 + (vt)^2]^{1/2}} \quad (3)$$

The zenith angle of nearest approach, α, is found from

$$\tan\alpha = \frac{a}{h-b} \quad (4)$$

Families of curves for $R = F_\theta/F_{\theta=\alpha}$ versus time at heights of 260 km and 800 km, for various values of α are shown in Fig. 5. The observations for the two lower satellites are given in Fig. 5a and the two higher in Fig. 5b. From the curves it can be seen that the data place tight constraints on the satellite heights and zenith angles of closest approach. The data for satellite A give $h = 260^{+40}_{-60}$ km and $\alpha = 10° \pm 10°$. The errors give the range of values of h and α permitted with 95% confidence. Counting statistics and telescope efficiencies are included. Circular satellite orbits are assumed and the reactor luminosities are considered constant. The data points are all to the left of the 300 km, $\alpha = 0°$ curve so the satellite cannot be as high as 300 km. An altitude of 200 km is excluded by the variation of the data points with time for the satellite passage. Satellite B is lower than 320 km and higher than 200 km for the same reasons given for satellite A.

Satellites C and D are clearly at higher altitudes. The above arguments put C below 900 km and D below 1050 km. Because the statistics get progressively worse for satellites A to B to C to D, it is not possible to distinguish a low height large α profile from one with a greater height and smaller α. If satellite C is placed at 800 km, α is constrained to 25° ± 5°, if at 500 km, to 57° ± 5°. For D at 800 km, α = 43° ± 5° and at 500 km, α = 63° ± 5°. Lower heights can be excluded by the large α required and the even larger θ where our efficiencies are low.

With these estimates of the satellite distances, flux measurements may be converted to luminosities. The gamma ray flux at the telescope and luminosity of satellite A were measured to be (9.6 ± 2.4) × 10^{-1} photons cm^{-2} s^{-1} and (6.1 ± 1.5) × 10^{15} photons s^{-1} above 0.3 MeV at the time when the distance from the telescope to the satellite was a minimum of 225 km. The errors are 1 standard deviation assuming the nominal satellite heights and angles above. The gamma-ray flux and luminosity for satellite B were measured to be (4.1 ± 1.0) × 10^{-1} photons cm^{-2} s^{-1} and (3.9 ± 1.0) × 10^{15} photons s^{-1} above 0.3 MeV. Satellite C gives (1.13 ± 0.28) × 10^{-1} photons cm^{-2} s^{-1} and (1.10 ± 0.28) × 10^{15} photons s^{-1} and satellite D gives (0.86 ± 0.21) × 10^{-1} photons cm^{-2} s^{-1} and (1.30 ± 0.32) × 10^{16} photons s^{-1}. Our best estimates of the properties of the satellites are given in Table 1, along with the telescope's latitude, longitude, and altitude.

On 15 April 1988, two RORSAT (Radar Ocean Reconnaissance Satellite) Soviet nuclear-powered satellites were in operation in low earth orbits: Cosmos 1900 and Cosmos 1932 (7). These are most likely the satellites A and B. Cosmos 1900 was launched in

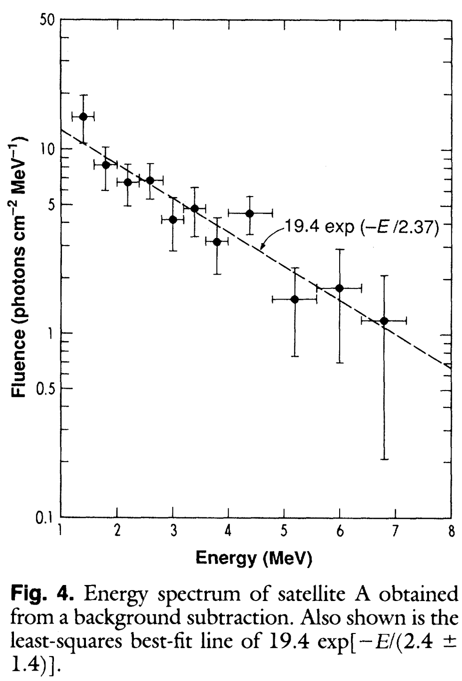

Fig. 4. Energy spectrum of satellite A obtained from a background subtraction. Also shown is the least-squares best-fit line of 19.4 exp[$-E$/(2.4 ± 1.4)].

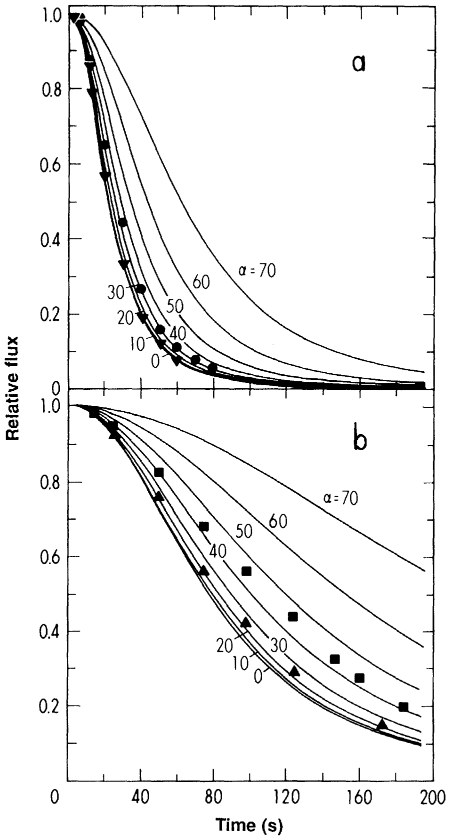

Fig. 5. Flux ratios $F_\theta/F_{\theta=\alpha}$, where F_θ is the value measured at zenith angle θ and $F_{\theta=\alpha}$ is the value at nearest approach, are shown for minimum zenith angles, α, of 0°, 10°, 20°, 30°, 40°, 50°, 60°, and 70°. (**a**) Data points for satellites A (▼) and B (●) are plotted for 260-km altitude. (**b**) Similarly, data points for satellites C (▲) and D (■) are for 800-km altitude.

December 1987 and Cosmos 1932 in March 1988. These satellites are in nearly circular orbits 260 km above the earth (*8, 10*). Their purpose is to locate large surface vessels and concentrations of smaller ships through active illumination by radar energy. The Soviet Union is the only nation that utilizes moderated nuclear reactors for power on satellites. In January 1989 the Soviets announced that at least two advanced-type reactors were placed in higher orbits in the preceding 2 years (*11*). These satellites are the most efficient, long-lived, and powerful ever put in orbit. These are most likely satellites C and D.

The UCR Telescope has the capability of detecting an A-type satellite reactor passing overhead at a distance of 2500 km with 5 σ significance. The longer observation time of reactors in the higher orbits partially counters the inverse square decrease in intensity. For locations other than overhead, the telescope's off-axis area factor and flatter time profile decrease the maximum satellite observation distance. The atmospheric attenuation difference between overhead and large zenith angles plays a minimal role with the balloon at 35-km altitude.

From Table 1 it can be seen that reactors in space may cause significant problems by increasing backgrounds, particularly for gamma-ray bursts. While precautions may be taken to program detectors to ignore these events, particularly for balloon observations, it may be more difficult to eliminate these events with satellite experiments.

REFERENCES AND NOTES

1. M. M. Waldrop, *Science* **242**, 1119 (1988).
2. C. Knox, *Sci. News* **134**, 340 (1988).
3. J. Primack, *et al.*, *Science and Global Security*, in press.
4. T. J. O'Neill, W. E. Sweeney, O. T. Turner, A. D. Zych, R. S. White, *IEEE Trans. Nuc. Sci.* **NS-35**, 511 (1987).
5. J. Simone, T. O'Neill, O. T. Turner, A. D. Zych, *ibid.* **NS-32**, 124 (1985).
6. R. Vandenbosch and J. Huizenga, *Nuclear Fission* (Academic Press, New York, 1973), p. 360.
7. S. Aftergood, *Space Policy* **5**, 25 (1989).
8. *Aviat. Week Space Technol.* **123**, 18 (19 August 1985).
9. T. D. Thompson, *TRW Space Log 1957–1987* (TRW Space & Technology Group, El Segundo, CA, 1988).
10. N. Johnson, *The Soviet Year in Space 1987* (Teledyne Brown Engineering, Denver, CO, 1988), pp. 69–75.
11. W. J. Broad, *New York Times*, 15 January 1989, p. A1.

12. We thank NASA for valuable support from grant NGR-05-008-022 and the National Scientific Balloon Facility for their field, balloon launch, and recovery operations support.

26 January 1989; accepted 13 March 1989

Hydrogen Sulfide on Io: Evidence from Telescopic and Laboratory Infrared Spectra

DOUGLAS B. NASH AND ROBERT R. HOWELL

Evidence is reported for hydrogen sulfide (H_2S) on Io's surface. An infrared band at 3.915 (± 0.015) micrometers in several ground-based spectra of Io can be accounted for by reflectance from H_2S frost deposited on or cocondensed with sulfur dioxide (SO_2) frost. Temporal variation in the occurrence and intensity of the band suggests that condensed H_2S on Io's surface is transient, implying a similar variation of H_2S abundance in Io's atmosphere. The band was observed in full-disk measurements of Io at several orbital longitudes, including once at 24° (~0.5 hour after Io's reappearance after an eclipse)—but not after another reappearance at 22°—and once at 95° (on Io's leading hemisphere). These results suggest that condensed H_2S is sparse and variable but can be widespread on Io's surface. When present, it would not only produce the infrared band but would brighten Io's typical surface at ultraviolet and visible wavelengths.

PLANETARY SCIENTISTS HAVE LONG suspected that H_2S is present on Io. Recently published infrared (IR) spectra (*1*) may contain positive evidence for H_2S. Early visible-wavelength spectroscopic studies of Io suggested that elemental sulfur was a major surface constituent (*2, 3*) and a principal component in the Io torus (*4*). Because Io is immersed in Jupiter's radiation belts, it was thought that proton bombardment of the sulfur-rich surface could form transient H_2S on Io and a tenuous but transient atmosphere (*5, 6*). The possibility of photodissociation of endogenic H_2S on Io by solar ultraviolet (UV) radiation was suggested (*7, 8*). Ground-based IR spectroscopic searches for atmospheric components including H_2S were negative (*9*) but were followed by Voyager's 1979 discovery of active volcanism (*10*) and the detection of ~0.2 cm-atm of SO_2 gas near Loki and the setting of an upper limit of ~0.07 cm-atm of H_2S gas in Io's atmosphere near the sunlight terminator (*11*).

Other ground-based observations had revealed distinct bands in Io's reflectance spectra near 4 μm (*12, 13*) that identified solid SO_2 on Io's surface (*6, 14*). Laboratory studies suggested that H_2S or SO_2 could be adsorbed on Io's surface (*15*). Variation in the depth and shape of Io's 4-μm band over several years of observations (*12, 16*) was later shown to be due to differences in the spatial distribution of SO_2 on Io rather than temporal variation in the SO_2 concentration (*17*). Searches for temporal variation in the SO_2 band strength at constant orbital longitude were negative (*1, 18*).

Apparent temporal variability in Io's spectrum was discovered by Howell *et al.* (*1*), who obtained several spectra showing a new band near 3.915 (± 0.015) μm (*19*). The band was moderately strong in Io spectra on several occasions but was usually absent or weak. Because these spectra showed discrepancies compared to most others and because

D. B. Nash, Jet Propulsion Laboratory, California Institute of Technology, Pasadena, CA 91109, and San Juan Capistrano Research Institute, San Juan Capistrano, CA 92675.
R. R. Howell, Department of Physics and Astronomy, University of Wyoming, Laramie, WY 82071.